Cut-and-paste restoration of entanglement transmission

Álvaro Cuevas,[1] Andrea Mari,[2] Antonella De Pasquale,[2] Adeline Orieux,[1,3] Marcello Massaro,[1,4] Fabio Sciarrino,[1] Paolo Mataloni,[1] and Vittorio Giovannetti[2]

[1]*Dipartimento di Fisica, Università di Roma La Sapienza, Rome, Italy*

[2]*NEST, Scuola Normale Superiore and Istituto Nanoscienze-CNR, 56127 Pisa, Italy*

[3]*LIP6, CNRS, Université Pierre et Marie Curie, Sorbonne Universités, 75005 Paris, France and IRIF, CNRS, Université Paris Diderot, Sorbonne Paris Cité, 75013 Paris, France*

[4]*Integrated Quantum Optics Group, Applied Physics, University of Paderborn, 33098 Paderborn, Germany*

(Received 2 February 2017; published 11 July 2017)

The distribution of entangled quantum systems among two or more nodes of a network is a key task at the basis of quantum communication, quantum computation, and quantum cryptography. Unfortunately, the transmission lines used in this procedure can introduce so many perturbations and so much noise in the transmitted signal that they prevent the possibility of restoring quantum correlations in the received messages either by means of encoding optimization or by exploiting local operations and classical communication. In this work we present a procedure which allows one to improve the performance of some of these channels. The mechanism underpinning this result is a protocol which we dub *cut and paste*, as it consists in extracting and reshuffling the subcomponents of these communication lines, which finally succeed in correcting each other. The proof of this counterintuitive phenomenon, while improving our theoretical understanding of quantum entanglement, also has a direct application in the realization of quantum information networks based on imperfect and highly noisy communication lines. A quantum optics experiment, based on the transmission of single-photon polarization states, is also presented which provides a proof-of-principle test of the proposed protocol.

DOI: 10.1103/PhysRevA.96.012314

I. INTRODUCTION

Reliable quantum communication channels [1,2] are crucial for all quantum information and computation protocols [3] where quantum data must be faithfully and efficiently transmitted among different nodes of a network [4], usually via traveling optical photons [5,6]. Typical applications are quantum teleportation [7], cryptography [8], and distributed quantum computation [9].

According to quantum mechanics, two systems can be prepared in an entangled state characterized by extraordinary correlations that are beyond any classical description [10]. A key objective in quantum communication is the distribution of such entanglement between two parties, say Alice and Bob. This can be easily achieved with perfect quantum channels: Alice entangles two systems and sends one of them to Bob. Even if the channel is not perfect, a fraction of the initial entanglement can still survive the transmission process and may be successively amplified by distillation protocols [11]. In principle, this technique allows for efficient entanglement distribution along a network of quantum repeaters connected by imperfect channels [12,13].

The situation is completely different for *entanglement-breaking* (EB) channels [14], which are so leaky and noisy that entanglement is always destroyed for every choice of the initial state. Such communication lines behave essentially as classical *measure-and-reprepear* operations [15]. In this case the previous techniques based on entanglement distillation and quantum repeaters cannot be applied simply because, after the transmission process, there is nothing left to distill or to amplify. Furthermore, any other error-correction protocol, based on pre- and postprocessing operations [16–19] or decoherence-free subspaces [20,21], is clearly ineffective since entanglement cannot be created out of separable states exploiting only local operations and classical communication. Other techniques introduced to cope with decoherence and dissipation, such as dynamical decoupling and bang-bang control techniques [22–24], while being potentially convenient for preserving static quantum memories [25], are instead impractical for systems physically traveling along a quantum channel. Indeed, such methods would require us to continuously modulate the Hamiltonian of the system during the transmission line where, usually, Alice and Bob have no direct access; moreover, these techniques are effective only in the non-Markovian regime in which the relaxation time of the environment is larger the time scale of the control operations. Non-Markovian memory effects have also been used in [26] to restore entanglement, but this is possible only if the environment degrees of freedom are directly accessible to Bob.

In this work we present an approach, which we dub *cut-and-paste*, that focuses on the way a given channel is assembled, proving that is possible to build reliable communication lines by starting from extremely noisy components. Specifically, we show, both theoretically and experimentally, that it is possible to restore the transferring of quantum correlations along a communication line of fixed length by simply splitting it into smaller pieces and by reorganizing them to form a new channel of the same length which is less noisy than the original one. The idea is exemplified in the top panel of Fig. 1. Here the map $\mathcal{M}$ associated with a communication line that connects two distant parties over a certain distance is represented as an ordered sequence of smaller elements, i.e., $\mathcal{M} = \Phi_N \circ \Phi_{N-1} \circ \cdots \circ \Phi_2 \circ \Phi_1$, where for $n = 1, \ldots, N$, Φ_n is the transformation which propagates the messages on the nth section of the line. Now assume that $\mathcal{M}$ is EB: accordingly, it will prevent the transferring of any form of quantum correlations. Yet in what follows we are going to show that there are cases where, by simply reshuffling the order in which the subchannels are connected to each other, we can

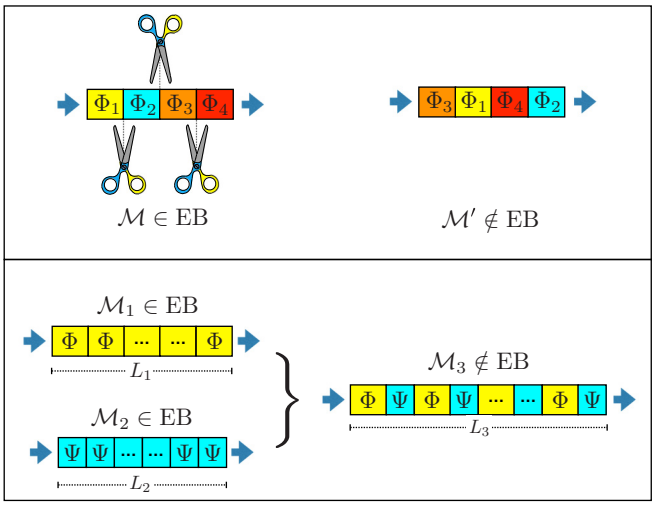

FIG. 1. Top: Pictorial representation of the cut-and-paste technique. The original communication channel $\mathcal{M}$ is entanglement breaking. By dividing it into smaller sections represented by the maps Φ_1, Φ_2, Φ_3, and Φ_4 and recombining them in the proper order we construct a new communication line $\mathcal{M}'$ which is less noisy than the original one; in particular, it is not entanglement breaking. Bottom: Merging of two spatially homogeneous EB channels, $\mathcal{M}_1$ and $\mathcal{M}_2$, to form the non-EB map $\mathcal{M}_3$.

create a new physical map $\mathcal{M}' = \Phi_{i_N} \circ \Phi_{i_{N-1}} \circ \cdots \circ \Phi_{i_2} \circ \Phi_{i_1}$ that does not suffer from such limitations (with $i_1, i_2, \ldots, i_N$ being a permutation of the first N natural numbers). From a practical point of view, this could, for instance, correspond to having a noisy transmission link of a given length, e.g., an optical fiber, which is entanglement breaking. In this case the cut-and-paste mechanism exactly prescribes a sequence of real physical operations to be performed on the transmission medium: dividing it in smaller pieces and reordering them. An interesting application of this effect is presented in the bottom panel of Fig. 1. Here we are in the presence of two communication lines, $\mathcal{M}_1$ and $\mathcal{M}_2$, of lengths L_1 and L_2, respectively, which are both EB and which, for the sake of simplicity, we assume to be spatially homogeneous. As we shall see in the next sections, there are situations in which we can create a new communication line $\mathcal{M}_3$ which allows one to reliably propagate quantum coherence over distances L_3 much larger than $L_1 + L_2$ by simply alternating pieces of the original maps, i.e.,

$$\mathcal{M}_3 = (\Phi \circ \Psi) \circ (\Phi \circ \Psi) \circ \cdots \circ (\Phi \circ \Psi) \notin \text{EB}, \qquad (1)$$

with Φ (Ψ) being the subchannel that composes $\mathcal{M}_1$ ($\mathcal{M}_2$) and the maximum value of L_3 being a function of the size of the pieces we have selected.

The cut-and-paste effect detailed above ultimately relies on the noncommutative character of quantum mechanics, in which it is not just the kinds of operations performed on a system that matter but also the order in which they are carried out. At variance with previous applications, here such a peculiar aspect of the theory exhibits its full potential impact by allowing or not allowing a well-defined operational task (i.e., the sharing of entanglement among distant parties). On a more practical ground, our results can find applications in the realization of quantum networks connected by highly damping and noisy communication links. More generally, they suggest an alternative way of engineering quantum devices, widening the possibilities of optimizing their performances by simply reordering the elements which constitute them.

In what follows we review some basic facts about EB maps and discuss the cut-and-paste mechanism by focusing on two examples: the first regards amplitude-damping and phase-damping channels operating on a qubit [3]; the second instead deals with a continuous model in which the propagation of signals in a noisy environment is represented in terms of effective master equations. Then for the amplitude-damping example we present an experimental test of this effect in which the qubits are encoded into the polarization degree of freedom of single photons.

II. THEORETICAL ANALYSIS

A quantum channel Φ is said to be EB if, when applied to one part of an entangled state, the output is always separable for every choice of the input [14]. Moreover, it can be shown that $\Phi \in$ EB if and only if, when operating locally on the system of interest S, it turns a maximally entangled state $|\Omega\rangle_{SA}$ of S and of an ancillary system A into a separable one [14], i.e.,

$$\rho_{SA}^{(\text{out})} = (\Phi \otimes \mathbb{I})(|\Omega\rangle_{SA}\langle\Omega|) \text{ is separable} \iff \Phi \in \text{EB}, \quad (2)$$

with $\mathbb{I}$ being the identity channel operating on A. A possible way to smooth the boundary between these "bad" channels and the "good" non-EB channel is the notion of EB *order* of a channel introduced in [27] and further studied in [28]. Accordingly, Φ is said to be EB of order n if it requires n consecutive applications to destroy the entanglement of any input state, i.e., if up to $n-1$ iterations of Φ are not EB while n (or more) iterations of Φ yield a EB transformation.

A. Cut-and-paste with discrete maps

Amplitude-damping (AD) channels are an important class of maps acting on a qubit [3]. They describe dissipation and decoherence processes of a two-level system in thermal contact with a zero-temperature external bath or the loss of a photon in the propagation of single-photon pulses along an optical fiber. Given an input density matrix ρ, the channel $\mathcal{A}_\eta$ transforms it as $\mathcal{A}_\eta(\rho) \equiv E_1 \rho E_1^\dagger + E_2 \rho E_2^\dagger$, where $E_1 \equiv \left[\begin{smallmatrix} 1 & 0 \\ 0 & \sqrt{\eta} \end{smallmatrix}\right]$ and $E_2 \equiv \left[\begin{smallmatrix} 0 & \sqrt{1-\eta} \\ 0 & 0 \end{smallmatrix}\right]$ are the Kraus operators expressed in the computational basis of the qubit and $\eta \in [0,1]$ is the transmission coefficient characterizing the map, interpolating between perfect transmission $\eta = 1$ and complete damping $\eta = 0$. One can easily verify that $\mathcal{A}_\eta$ is never EB for $\eta > 0$ and, from the semigroup property

$$\mathcal{A}_{\eta_2} \circ \mathcal{A}_{\eta_1} = \mathcal{A}_{\eta_1} \circ \mathcal{A}_{\eta_2} = \mathcal{A}_{\eta_2 \eta_1}, \qquad (3)$$

that it also has infinite order, i.e., $n = \infty$. Interestingly enough, however, it can be shown [27] that for sufficiently small values of the transmission coefficient η, the order of $\mathcal{A}_\eta$ can be reduced by applying suitable unitary gates after or before it. In particular one can identify (nonunique) unitary operations $\rho \to \mathcal{U}(\rho) = U \rho U^\dagger$ such that the channels

$$\Phi = \mathcal{A}_\eta \circ \mathcal{U}, \quad \Psi = \mathcal{U}^\dagger \circ A_\eta \qquad (4)$$

are both EB of order $n = m = 2$: for instance, this happens at $\eta = 0.3$ when we take the bit flip σ_x as U. What is more interesting, we can now use these maps to provide evidence of the cut-and-paste mechanism. Indeed, consider the compound map $\mathcal{M}$ formed by two applications of Φ and followed by two applications of Ψ, i.e., $\mathcal{M} = \Phi \circ \Phi \circ \Psi \circ \Psi$ (corresponding to set $\Phi_1 = \Phi_2 = \Phi$ and $\Phi_3 = \Phi_4 = \Psi$ in the top panel of Fig. 1). This is clearly EB; however, the alternate application of the two maps produces the AD channel of transmissivity η^4, which, as already stated, is never EB:

$$\begin{aligned}\mathcal{M}' &= \Phi \circ \Psi \circ \Phi \circ \Psi \\ &= \mathcal{A}_\eta \circ \mathcal{U} \circ \mathcal{U}^\dagger \circ \mathcal{A}_\eta \circ \mathcal{A}_\eta \circ \mathcal{U} \circ \mathcal{U}^\dagger \circ \mathcal{A}_\eta = \mathcal{A}_{\eta^4} \notin \text{EB}.\end{aligned} \tag{5}$$

Similar results can also be obtained by replacing the AD map $\mathcal{A}_\eta$ with the phase-damping (PD) channel $\mathcal{E}_p$ [3] in the above expressions. For $p \in [0,1]$ the latter transforms a generic input density matrix ρ of the qubit as $\mathcal{E}_p(\rho) \equiv 1/2[(1+p)\rho + (1-p)\sigma_z \rho \sigma_z]$, describing the loss of coherence between its energy eigenstates. Analogously to the AD maps, $\mathcal{E}_p \notin \text{EB}$ for $p > 0$ and satisfies the semigroup property $\mathcal{E}_{p_2} \circ \mathcal{E}_{p_1} = \mathcal{E}_{p_1} \circ \mathcal{E}_{p_2} = \mathcal{E}_{p_2 p_1}$, from which it immediately follows that they are EB of infinite order, i.e., $\mathcal{E}_p \in \text{EB}^n$ for $n = \infty$. Furthermore, also in this case for p sufficiently small, one can find a unitary transformation $\mathcal{U}$ such that the maps $\Phi = \mathcal{E}_p \circ \mathcal{U}$ and $\Psi = \mathcal{U}^\dagger \circ \mathcal{E}_p$ are EB of order 2, e.g., by fixing $p = 0.4$ and $U = 1/\sqrt{2}(\sigma_z - \sigma_x)$.

The examples presented here constitute also a clear proof-of-principle demonstration of the merging effect described in the bottom panel of Fig. 1. Indeed, in both the AD and the PD implementations, not only is the channel $\mathcal{M}$ EB, but also the maps associated with its first and second sections (i.e., maps $\mathcal{M}_1 = \Phi \circ \Phi$ and $\mathcal{M}_2 = \Psi \circ \Psi$, respectively) share the same property. Yet even though, individually, such transformations are both bad operations, when split and merged as in (5), they manage to somehow correct their detrimental effects. This is a curious instance of an effective quantum error-correction procedure obtained by properly mixing two different types of errors. Furthermore, due to their semigroup property, which both the AD and PD maps fulfill, the channel $\Phi \circ \Psi$ actually has an infinite order ($n = \infty$). Accordingly, the procedure can be iterated an arbitrary number of times, leading to an infinitely long sequence $(\Phi \circ \Psi) \circ (\Phi \circ \Psi) \circ \cdots$ which, nonetheless, can still transmit a nonzero fraction of entanglement (corresponding to having a divergent value of L_3 in Fig. 1).

B. Cut-and-paste with continuous channels

The potentiality of the cut-and-paste method is much more general and is not restricted to the idealized sequences of discrete unitary and dissipative operations discussed so far. In more realistic scenarios, like the continuous propagation of a quantum state along a physical medium, the transmission is better described by continuous homogeneous channels (also known as quantum dynamical semigroups) [29,30]. In this framework, the propagation of a signal for an infinitesimal distance dx induces a change in the density matrix according to a master equation of the form

$$\frac{d\rho}{dx} = \mathcal{L}(\rho), \tag{6}$$

where the linear Liouvillian operator $\mathcal{L}$ completely characterizes the channel and generates simultaneously the unitary and dissipative dynamics of the system [29,30]. The formal solution of Eq. (6) is $\rho(x) = e^{\mathcal{L}x}\rho(0)$ and represents the propagation of the quantum state for a finite length x along the physical medium.

Now, as in the case in the bottom panel of Fig. 1, assume that we have at our disposal two of these maps (e.g., two different wave guides) characterized by $\mathcal{L}_1$ and $\mathcal{L}_2$, such that the integrated dynamics becomes EB after a propagation length of $x = L_1$ and $x = L_2$, respectively, i.e.,

$$\mathcal{M}_1 = e^{\mathcal{L}_1 L_1} \in \text{EB}, \quad \mathcal{M}_2 = e^{\mathcal{L}_2 L_2} \in \text{EB}. \tag{7}$$

If we divide the two transmission lines into shorter pieces of length L_1/n_1 and L_2/n_2, we obtain the maps $\Phi = e^{\mathcal{L}_1 L_1/n_1}$ and $\Psi = e^{\mathcal{L}_2 L_2/n_2}$, which are, by construction, EB of order n_1 and n_2. The idea is thus to construct a new communication line using Φ and Ψ as elementary building blocks which are merged to form an alternate sequence as in Eq. (1) with the aim of increasing the entanglement propagation length as much as possible. As an example we can consider two hypothetical transmission lines, characterized by the following Liouvillian operators [29,30]:

$$\mathcal{L}_j(\rho) = -i[H_j, \rho] + \frac{\epsilon}{2}(2\sigma_- \rho \sigma_+ - \sigma_+ \sigma_- \rho - \rho \sigma_+ \sigma_-), \tag{8}$$

where $j = 1,2$, $H_1 = \Omega \sigma_x$, $H_2 = -\Omega \sigma_x$, and $\sigma_\pm = (\sigma_x \pm i\sigma_y)/2$. The first term in this equation induces a unitary rotation of the quantum state, while the second term is responsible for the dissipative dynamics. Accordingly, Eq. (8) is a sort of continuous analog of the discrete maps of Eq. (4) in which the two different forms of transformations (i.e., $\mathcal{A}_\eta$ and $\mathcal{U}$) are applied to the system not one after the other but simultaneously.

For nonzero values of Ω and ϵ, both channels become EB at the same finite propagation length L. For simplicity we cut slices of equal length L/n for both channels, and we paste them according to the alternating sequence given in Eq. (1). This new continuous channel is formally described by a master equation in which the Liouvillian operator switches between $\mathcal{L}_1$ and $\mathcal{L}_2$ after the propagation of L/n space intervals, i.e.,

$$\frac{d\rho}{dx} = \mathcal{L}_3^{(n)}(\rho) = \begin{cases} \mathcal{L}_1(\rho), & \left[\frac{x}{L/n}\right] = \text{even}, \\ \mathcal{L}_2(\rho), & \left[\frac{x}{L/n}\right] = \text{odd}, \end{cases} \tag{9}$$

where $[\cdot]$ is the integer part of the argument.

We now test the entanglement condition given in Eq. (2); that is, we study the entanglement evolution induced by the channel $\mathcal{L}_3^{(n)}$ when applied to one part of a maximally entangled state. The value of entanglement measured in terms of the concurrence [31] as a function of the distance x is represented in Fig. 2(a) for different values of n. We observe that with respect to the original channels $\mathcal{L}_1$ and $\mathcal{L}_2$, the new channels $\mathcal{L}_3^{(n)}$ become entanglement breaking at larger distances. Moreover, the entanglement propagation length increases with n and tends to infinity. This fact can be proved theoretically: using a simple Trotter decomposition argument,

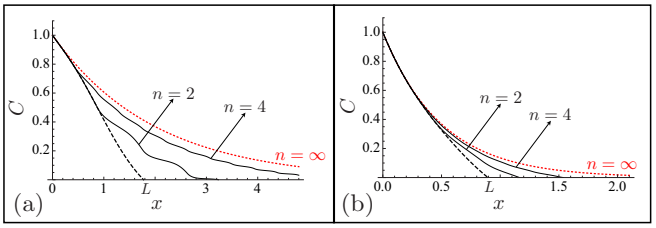

FIG. 2. Residual concurrence [31] as a function of the propagation distance x for different continuous channels. At $x = 0$ the system is initialized in the singlet state. (a) The rotating amplitude-damping channels defined in Eq. (8) (black dashed line) and their associated cut-and-paste improvements described in Eq. (9) for different values of n (black solid lines). The limit for $n \to \infty$ is also represented (red dotted line). (b) The rotating phase-damping channels defined in Eq. (10), with the notation being the same as in (a). The values of the parameters are $\Omega = 1.5$ and $\epsilon = 1$ for both panels, which yield $L = 1.75$ for Eq. (8) and $L = 0.85$ for Eq. (10) for the maximum propagation length that allows for quantum coherence preservation (beyond these values the maps become EB). The cut-and-paste approach allows us to significantly increase the EB threshold well beyond the original one: for instance, in the case of Eq. (8) setting $n = 2$ already gives L_3, which is more than twice the value of L [similarly, this happens also for the case of Eq. (10) by setting $n = 4$].

the dynamics for $n \to \infty$ tends to a pure amplitude-damping channel which is never entanglement breaking.

Exactly the same analysis and similar results are valid also for other continuous channels. For example, if we replace Eq. (8) with

$$\mathcal{L}_j(\rho) = -i[H_j,\rho] + \frac{\epsilon}{2}[\sigma_z,[\sigma_z,\rho]], \tag{10}$$

we obtain two propagation media indexed by $j = 1,2$ in which a qubit is rotated in different directions by $H_1 = \Omega\sigma_x$ and $H_2 = -\Omega\sigma_x$ while, at the same time, it is subject to a dephasing process [29,30]. Remarkably, this is a quite realistic model for the propagation polarization qubits in optical fibers, in which dephasing and polarization drift can simultaneously affect the transmitted photons. Figure 2(b) demonstrates that our approach is applicable also in this situation, obtaining a significant enhancement of the entanglement propagation distance.

III. EXPERIMENTAL IMPLEMENTATION

In this section we present a quantum optics experiment demonstrating the possibility of restoring the transmission of entanglement via the cut-and-paste technique previously described. Specifically, we study the transmission of a qubit encoded in the horizontal and vertical polarizations of a photon $\{|0\rangle \equiv |H\rangle, |1\rangle \equiv |V\rangle\}$, and inspired by Eq. (4), we take

$$\Phi = \mathcal{A}_{\eta_2} \circ \mathcal{U}_\theta, \quad \Psi = \mathcal{U}_\varphi \circ \mathcal{A}_{\eta_1}, \tag{11}$$

where now the unitary mappings $\mathcal{U}_\xi$, with $\xi = \theta,\varphi$, induce the rotation $U_\xi \equiv \left[\begin{smallmatrix} \cos(2\xi) & \sin(2\xi) \\ \sin(2\xi) & -\cos(2\xi) \end{smallmatrix}\right]$ in the polarization degree of freedom of the photon.

The experimental setting is sketched in Fig. 3: for assigned values of η_1, η_2, θ, and φ, it is designed to study the presence or absence of entanglement on a maximally polarization entangled state $|\Omega\rangle_{SA}$ of a two-photon pair, which evolves under the transformation (2) given by the channels $\mathcal{M}' = \Phi \circ \Psi \circ \Phi \circ \Psi$, $\mathcal{M}_1 = \Phi \circ \Phi$, and $\mathcal{M}_2 = \Psi \circ \Psi$ by properly tuning the parameters of the interferometer (see below for details). For each one of these three choices the EB character of the transformation is hence determined by exploiting the equivalence (2) by measuring the concurrence [31] of the associated density matrix $\rho_{SA}^{(\mathrm{out})}$ through full tomography performed at the output of the setup: evidence of the cut-and-paste effect is thus obtained whenever one notices a nonzero value for the concurrence for $\mathcal{M}'$ along with a zero concurrence value for $\mathcal{M}_1$ and $\mathcal{M}_2$.

In our test we employ as $|\Omega\rangle_{SA}$ the superpositions $(|H\rangle_S|V\rangle_A + e^{i\phi}|V\rangle_S|H\rangle_A)/\sqrt{2}$ created through a high-brilliance, high-purity polarization entanglement source (see [32]). The source consists of a nonlinear periodically poled potassium titanyl phosphate ($KTiOPO_4$) crystal pumped by a single-mode laser at 405 nm and 2.75 mW of power within a Sagnac interferometer (SI) and able to generate pairs of photons in the system mode S and the ancillary mode A at 810 nm by type-II parametric down-conversion. The generated pairs (more than 50 000 detected coincidences per second) have a coherence length of $L_{\mathrm{coh}} = 1.02$ mm and spectral bandwidth $\Delta\lambda = 0.43$ nm. The ancillary photon A is hence directly transmitted to a detector station, while the photon S is connected to the testing area which implements the action of the maps $\mathcal{M}'$, $\mathcal{M}_1$, and $\mathcal{M}_2$ through both free-space and fiber-optic links and then sent to a second detector station (see Fig. 3).

When emerging from the source, the resulting state has more than 98% fidelity with the target $|\Omega\rangle_{SA}$ and concurrence equal to $C = 0.98$, corresponding to an effective $C = 0.94$ at the interferometer detectors because of the unavoidable entanglement degradation occurring in the connection with the testing channel (see Appendix B).

The mappings $\mathcal{U}_\xi$ entering (11) are implemented by placing properly oriented half-wave plates (HWPs) along the optical axis of the propagating photons. The AD channels $\mathcal{A}_{\eta_1}$ and $\mathcal{A}_{\eta_2}$ are instead realized by means of a dual interferometric setup (DIF) obtained by putting two independent polarization controls inside a displaced SI, coupled to an external unbalanced Mach-Zehnder interferometer (MZI; see Appendix A for more details).

To implement $\mathcal{M}' = \Phi \circ \Psi \circ \Phi \circ \Psi$ we exploit the semigroup property (3) to formally express the product $\mathcal{A}_{\eta_1} \circ \mathcal{A}_{\eta_2}$ as a single AD channel with damping parameter $\eta_2\eta_1$. Accordingly, we write

$$\mathcal{M}' = \mathcal{A}_{\eta_2} \circ \mathcal{U}_\theta \circ \mathcal{U}_\varphi \circ \mathcal{A}_{\eta_1\eta_2} \circ \mathcal{U}_\theta \circ \mathcal{U}_\varphi \circ \mathcal{A}_{\eta_1}. \tag{12}$$

This simple trick enables us to implement the whole transformation by means of only three DIFs instead of four (one for each AD map entering the original sequence) by setting the parameters α_1, $\alpha_{2,1}$, and α_2 in Fig. 3 equal to $\arccos(-\sqrt{\eta_1})/2$, $\arccos(-\sqrt{\eta_2\eta_1})/2$, and $\arccos(-\sqrt{\eta_2})/2$, respectively [see Eq. (A2) in Appendix A]. For fixed values of η_2 and θ, the action of $\mathcal{M}_1 = \Phi \circ \Phi$ is studied by deactivating both Ψ maps in (12). Such an operation is realized in two steps. First, the HWP placed in the internal vertically polarized path of the first DIF of Fig. 3 is set to $\alpha_1 = \pi/2$ to simulate $\eta_1 = 1$,

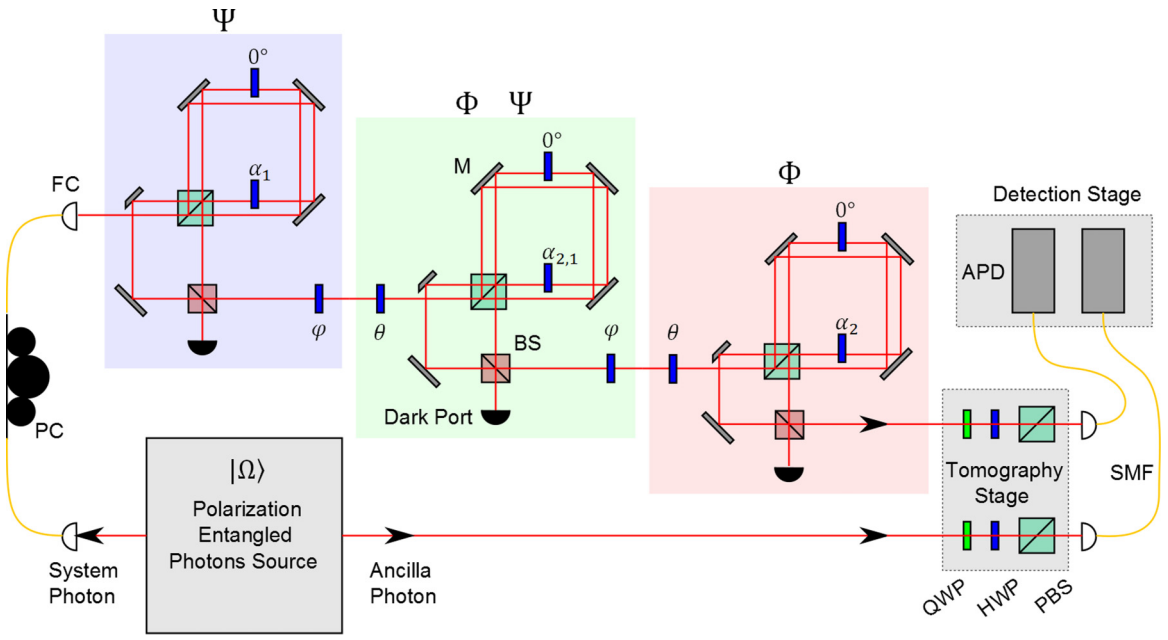

FIG. 3. Scheme of the experimental setup. The A photon belonging to the polarization entangled state $|\Omega\rangle_{SA}$ is directly linked to the detector, while the S photon is connected to the three DIFs via a single-mode optical fiber (SMF). A bipartite full tomography stage, given by one HWP and one quarter-wave plate (QWP) for both the system and the ancilla photons, allows us to reconstruct the density matrix of the two-photon state. Finally, photons pairs are coupled to two electronically synchronized avalanche photodiodes (APDs) through two SMFs. PC: polarization controller. BS and PBS: beam splitter and polarizing beam splitter.

while the HWPs placed in the internal vertically polarized paths of the second and third DIFs are set to induce the same rotation [i.e., $\alpha_{2,1} = \alpha_2 = \arccos(-\sqrt{\eta_2})/2$]. Second, both the external HWPs in Fig. 3 which are responsible for the implementation of $\mathcal{U}_\varphi$ are simply taken out of the setup. Similarly, for each given value of η_1 and φ, we can study the action of $\mathcal{M}_2 = \Psi \circ \Psi$ deactivating both Φ maps by taking out of the setup both the external HWPs associated with the rotation $\mathcal{U}_\theta$ and by setting the internal HWPs of the three DIFs as $\alpha_1 = \alpha_{2,1} = \arccos(-\sqrt{\eta_1})/2$ and $\alpha_2 = \pi/2$ to simulate $\eta_2 = 1$. Finally, the implementation of the identity channel (useful for directly measuring the net entanglement of the input state available at the detectors of the interferometer) is obtained by setting $\alpha_1 = \alpha_{2,1} = \alpha_2 = \pi/2$ and removing all the external HWPs.

In Fig. 4 we report the results obtained after setting the transmission coefficients of the AD channels entering Eq. (11) at $\eta_1 = \eta_2 = 0.3$ (the value for which we have already anticipated the possibility of witnessing the cut-and-paste effect). In particular Figs. 4(a) and 4(b) show the EB analysis for maps $\mathcal{M}_1 = \Phi \circ \Phi$ and $\mathcal{M}_2 = \Psi \circ \Psi$ when θ and φ are varied, respectively. In both cases one may notice that the concurrences of the associated SA output states (2) nullify when these angles reach the values $\pm\pi/4$, implying that under these conditions the channels Φ and Ψ are EB of order 2. Figure 4(c) shows instead the EB analysis for the map $\mathcal{M}'$ of Eq. (12) when the angle φ is kept constant at $\frac{\pi}{4}$ and θ is varied: one notices that the concurrence of the output state (2) is peaked and different from zero around $\theta = \pm\pi/4$, indicating that for these values the map is not EB. Hence, our data provide clear experimental evidence of the cut-and-paste entanglement-restoring effect for $\eta_1 = \eta_2 = 0.3, \theta = \pm\pi/4$, and $\varphi = \pm\pi/4$. The theoretical prediction corresponding to the red curves shown in Fig. 4 was obtained by taking into account the actual optical elements of the experimental setup: the slight residual disagreement being mainly due to the unavoidable difficulties of coupling different polarization and path contributions within the same single-mode fiber (see Appendix B for details).

IV. CONCLUSIONS

"Cutting" two entanglement-breaking channels into two or more pieces and properly reordering the corresponding parts can yield a new communication line which is not entanglement breaking: this is the essence of the cut-and-paste protocol. In this work we gave a theoretical proposal for both discrete and continuous time evolution, the latter proving a more realistic model for signal evolution within a piece of material. We considered as benchmarks for a proof-of-principle demonstration the rotated amplitude- and phase-damping maps. In the second part of the paper, we focused on the discrete amplitude-damping evolution, yielding an experimental demonstration of this quite unconventional protocol. The quantum optics experiment that we realized is based on the transmission of photon polarization qubits and has unambiguously proved the predicted entanglement recovery effect. The specific proof-of-principle demonstration was constructed using combinations of amplitude-damping channels and unitary operations. However, the proposed cut-and-paste technique is not limited to this scenario and can also be applied to more general single-qubit channels. We also envisage interesting generalizations of our approach to arbitrary multiqubit channels [2] and to the physically important class of Gaussian entanglement-breaking channels [33,34].

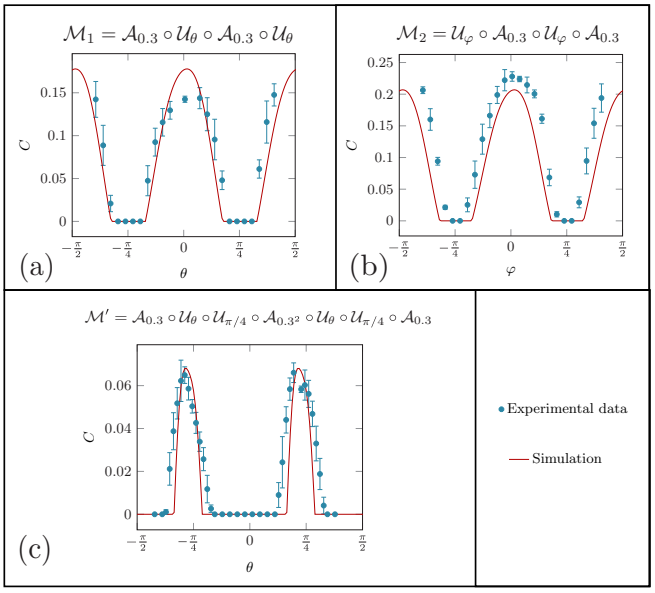

FIG. 4. Entanglement-breaking analysis for the maps $\mathcal{M}_1 = \Phi \circ \Phi$, $\mathcal{M}_2 = \Psi \circ \Psi$, and $\mathcal{M}' = \Phi \circ \Psi \circ \Phi \circ \Psi$ obtained by cascading the channels of Eq. (11) with $\eta_1 = \eta_2 = 0.3$. (a) Functional dependence upon the angle θ of the concurrence C of the state (2) at the output channel $\mathcal{M}_1$ obtained from the scheme in Fig. 3 by setting $\alpha_1 = \pi/2$, $\alpha_{2,1} = \alpha_2 = \arccos(-\sqrt{\eta_2})/2$ and removing the rotations $\mathcal{U}_\varphi$ (see text). For θ around $\pm\pi/4$ the system exhibits zero concurrence, showing that $\Phi \circ \Phi$ is EB or, equivalently, that Φ is EB of order 2. (b) Functional dependence upon the angle φ of the concurrence C of the state (2) at the output channel $\mathcal{M}_2$ obtained by setting $\alpha_1 = \alpha_{2,1} = \arccos(-\sqrt{\eta_1})/2$ and $\alpha_2 = \pi/2$ and removing the rotations $\mathcal{U}_\theta$. Like in the previous case, for φ around $\pm\pi/4$ the system exhibits zero concurrence, showing that $\Psi \circ \Psi$ is EB or, equivalently, that Ψ is EB of order 2. (c) Functional dependence upon the angle θ of the concurrence C of the state (2) at the output channel $\mathcal{M}'$ obtained by setting $\alpha_1 = \alpha_2 = \arccos(-\sqrt{0.3})/2$, $\alpha_{2,1} = \arccos(-0.3)/2$ and keeping $\varphi = \frac{\pi}{4}$. In all plots the red curves represents the theoretical prediction obtained by considering the actual experimental conditions (see Appendix B). Each point and the associated statistical error were taken from a set of N measurements ($3 \leqslant N \leqslant 11$) under equivalent mode-coupling conditions.

Our technique and its experimental realization demonstrate the real possibility of recovering some amount of entanglement or extending its distance distribution over extremely noisy links, opening a novel opportunity towards the realization of quantum information networks of increasing complexity [35,36]. Moreover, the unusual entanglement recovery effect studied in this work is also interesting in its own right and could open new research lines in quantum channel theory [2] and error-correction protocols [18].

ACKNOWLEDGMENTS

This work was supported by the ERC-Starting Grant 3D-Quest (3D-Quantum Integrated Optical Simulation; Grant Agreement No. 307783). It was also partially supported by the ERC through the Advanced Grant No. 321122 SouLMan and by "Becas Chile", a PhD scholarships program of the Chilean agency Comisión Nacional de Investigación Científica y Tecnológica (CONICYT).

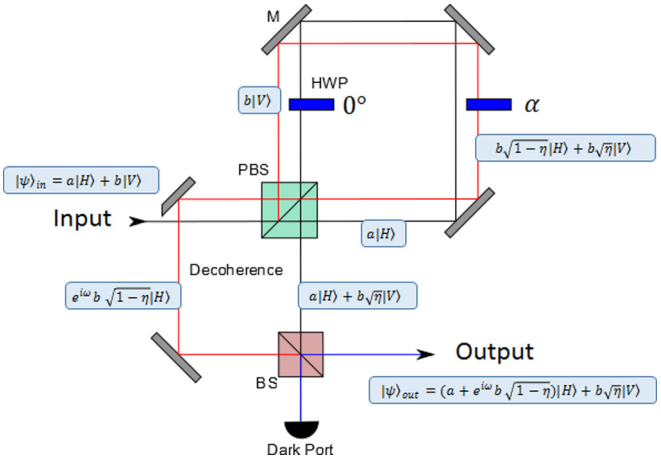

FIG. 5. Scheme of the experimental implementation of the AD map $\mathcal{A}_\eta$ via a DIF loop. In this picture path **a**, associated with the $|H\rangle$ polarization component, is indicated in black, while path **b**, associated with the $|V\rangle$ component, is in red. The blue elements represent HPW elements.

APPENDIX A: AMPLITUDE-DAMPING CHANNEL

In the polarization basis $\{|H\rangle, |V\rangle\}$ the action of the AD map $\mathcal{A}_\eta$ can be realized by means of the DIF in Fig. 5. Here an incoming signal $|\psi\rangle = a|H\rangle + b|V\rangle$ enters first a Sagnac interferometer realized by means of a polarizing beam splitter (PBS), which allows us to split the two polarization components by mapping them into two distinct optical paths, i.e., path **a**, the black path in Fig. 5, for the $|H\rangle$ component and path **b**, the red path, for the $|V\rangle$ component. Accordingly, the state of the signal immediately after the PBS can be expressed as $a|H\rangle \otimes |\mathbf{a}\rangle + b|V\rangle \otimes |\mathbf{b}\rangle$, where we expanded the Hilbert space by explicitly adding the path degrees of freedom. Inserting then a rotated HWP along **b**, a rotation on the polarization degree of freedom of $|V\rangle \otimes |\mathbf{b}\rangle$ can then be induced while leaving the polarization of the $|H\rangle \otimes |\mathbf{a}\rangle$ unchanged, i.e., $|V\rangle \otimes |\mathbf{b}\rangle \to \sqrt{\eta}|V\rangle \otimes |\mathbf{b}\rangle + \sqrt{1-\eta}|H\rangle \otimes |\mathbf{b}\rangle$ and $|H\rangle \otimes |\mathbf{a}\rangle \to |H\rangle \otimes |\mathbf{a}\rangle$, with the unitary operator responsible for such a transformation being

$$U_0 \otimes |\mathbf{a}\rangle\langle\mathbf{a}| + U_{\alpha(\eta)} \otimes |\mathbf{b}\rangle\langle\mathbf{b}|, \tag{A1}$$

where

$$\alpha(\eta) = \arccos(-\sqrt{\eta})/2 \tag{A2}$$

and for α generic U_α indicates the polarization rotation associated with a HWP element rotated by α, which in the basis $|H\rangle$, $|V\rangle$ is represented by the matrix

$$U_\alpha = \begin{bmatrix} \cos(2\alpha) & \sin(2\alpha) \\ \sin(2\alpha) & -\cos(2\alpha) \end{bmatrix} \tag{A3}$$

[as indicated in Fig. 5, an unrotated HWP, performing the unitary transformation U_0 in Eq. (A1), was also inserted in path **a** in order to preserve the temporal coherence between the two counterpropagating beams].

Subsequently, on their second encounter with the PBS, the two signals enter an unbalanced Mach-Zehnder interferometer which separates the horizontal component of path **b**, adding to it a random phase $e^{i\omega}$ before recombining the signals at a 50:50 beam splitter (BS). Accordingly, with a probability of 1/2 the state emerging from the output port of the figure is described by the vector $|\psi\rangle_{\rm out} = (a + e^{i\omega} b\sqrt{1-\eta})|H\rangle + b\sqrt{\eta}|V\rangle$, which, upon averaging over the random term ω, corresponds to the action of $\mathcal{A}_\eta$ on $|\psi\rangle$, with no photon emerging otherwise (in writing $|\psi\rangle_{\rm out}$ the path degree of freedom has been removed since the BS effectively filters out one of them).

In the experimental setting shown in Fig. 3 the above transformation is iterated three times in order to reproduce the sequences of maps Ψ and Φ as detailed in the main text, with the precaution of setting the physical dimensions of the associated Mach-Zehnder interferometers to be different from each other in order to avoid any spurious coherence among the random phases they are meant to introduce.

APPENDIX B: SIMULATION OF THE SCHEME

The complexity of the geometry and the difficulties of coupling many spatial modes within one final single-mode fiber affect the entanglement preservation even if the maps implemented by the various DIF were set to operate as identity channels [i.e., taking $\eta_1 = \eta_2 = 1$ in Eq. (12), which implies setting $\alpha_1 = \alpha_{2,1} = \alpha_2 = 0$, and physically removing the HWPs implementing the unitary rotations $\mathcal{U}_\varphi$ and $\mathcal{U}_\theta$]. Indeed, under such experimental conditions, the mean entanglement degradation on each DIF was greater than 1.3%; thus, the maximum concurrence at the end of the entire sequence of channels decreases from 98% to 94%. Besides the decrease in entanglement, the number of coincidences per second was also affected, considering that the effective photon transmission of each double interferometer was $\sim$1/3. Furthermore, the effective operation of each interferometer, and therefore of each channel, can differ considerably from the others, even for small differences of the optical elements.

The numerical simulations presented in Fig. 4 were obtained by taking into account all these imperfections. In particular we consider as an input to the setup an effective input state of Werner form, $\rho_{SA} = W|\Omega\rangle_{SA}\langle\Omega| + (1-W)\mathbb{I}_{SA}/4$, with the parameter $W \in [0,1]$ extrapolated from the degree of entanglement of the source. Regarding the BS transformations, instead, we describe them as the following 2×2 matrices with respect to the spatial degree of freedom associated with the input ports:

$$B = \begin{bmatrix} \sqrt{T'} & i\sqrt{R'} \\ i\sqrt{R'} & \sqrt{T'} \end{bmatrix}, \tag{B1}$$

where the measured optical transmissivity T and reflectivity R have been renormalized to include losses $L = 1 - T - R$ by setting $T' = T/(1-L)$ and $R' = R/(1-L)$ (the average values of our set of BSs being $T = 0.48$, $R = 0.44$, and $L = 0.08$). Analogously, to simulate the PBSs, we separated the action of each one of them into two BS-like operations, one for horizontally polarized light and one for vertically polarized light; that is, adopting the notation introduced in (A1), we describe them in terms of the following unitary transformation:

$$|H\rangle\langle H| \otimes B_H + |V\rangle\langle V| \otimes B_V. \tag{B2}$$

Here B_H and B_V are operators coupling vectors $|\mathbf{a}\rangle$ and $|\mathbf{b}\rangle$ as in (B1) with normalized transmissivities T'_H and T'_V and reflectivities R'_H and R'_V, connected with the corresponding optical values T_H, T_V, R_H, and R_V via the associated losses L_H and L_V. These parameters have been characterized experimentally by using a cw diode laser with the same wavelength (810 nm) as the expected entangled photons, obtaining, on average, over the set of the PBSs employed in the experiment, the values $T_H = 0.965$, $R_H = 0.0185$, and $L_H = 0.022$ ($T_V = 0.004$, $R_V = 0.948$, and $L_V = 0.048$).

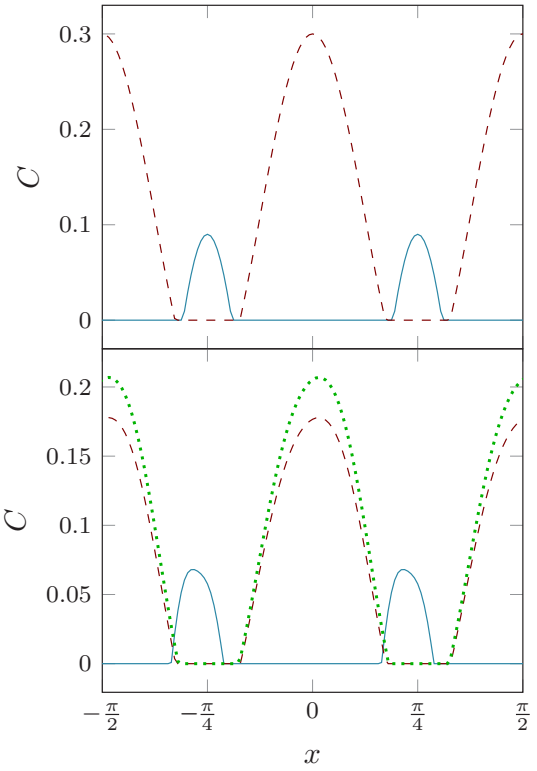

FIG. 6. Top: Concurrence values at the output of the scheme in Fig. 3 obtained assuming ideal conditions. The blue curve gives C for the map $\mathcal{M}' = \Phi \circ \Psi \circ \Phi \circ \Psi$ in Eq. (12) obtained by rotating the angle $x = \theta$ with φ fixed at $\frac{\pi}{4}$; the red dashed curve represents instead the value of C for the channel $\mathcal{M}_1 = \Phi \circ \Phi$ or $\mathcal{M}_2 = \Psi \circ \Psi$, obtained by rotating the angle $x = \theta$ or $x = \varphi$, respectively. Bottom: Same plots as in the top panel obtained using real optical-element simulations. Also in this case the blue curve represents $\mathcal{M}'$ obtained by rotating the angle $x = \theta$ with φ fixed at $\frac{\pi}{4}$; the red dashed curve represents instead $\mathcal{M}_1$, obtained by rotating the angle $x = \theta$, while the green dotted curve represents $\mathcal{M}_2$, obtained by rotating the angle $x = \varphi$. All the curves have been produced by setting the transmission coefficients of the active AD channels equal to $\eta = 0.3$.

In Fig. 6 we report a comparison between the ideal theoretical behavior of the output concurrences C and the corresponding simulated values obtained by rescaling the setup parameters as detailed above. Apart from finding degraded values of C, one notices that the simulated values present a clear difference in the behavior of $\mathcal{M}_1$ and $\mathcal{M}_2$ and a crooked asymmetry in the concurrence peaks of $\mathcal{M}'$ which

are not present in the ideal theoretical curves but which are clearly evident in the experimental data in Fig. 4. The residual disagreement between the latter and the simulations must be attributed to the different fiber-coupling efficiencies of all 27 possible polarization-path modes, which are difficult to chart due to mechanical random fluctuations of the setting.

[1] J. P. Gordon, Proc. IRE **50**, 1898 (1962).
[2] A. S. Holevo, *Quantum Systems, Channels, Information: A Mathematical Introduction* (De Gruyter, Berlin, 2012).
[3] M. A. Nielsen and I. L. Chuang, *Quantum Computation and Quantum Information* (Cambridge University Press, Cambridge, 2010).
[4] H. J. Kimble, Nature (London) **453**, 1023 (2008).
[5] L. M. Duan, M. D. Lukin, J. I. Cirac, and P. Zoller, Nature (London) **414**, 413 (2001).
[6] C. M. Caves and P. B. Drummond, Rev. Mod. Phys. **66**, 481 (1994).
[7] C. H. Bennett, G. Brassard, C. Crépeau, R. Jozsa, A. Peres, and W. K. Wootters, Phys. Rev. Lett. **70**, 1895 (1993).
[8] N. Gisin, G. Ribordy, W. Tittel, and H. Zbinden, Rev. Mod. Phys. **74**, 145 (2002).
[9] A. Serafini, S. Mancini, and S. Bose, Phys. Rev. Lett. **96**, 010503 (2006).
[10] R. Horodecki, P. Horodecki, M. Horodecki, and K. Horodecki, Rev. Mod. Phys. **81**, 865 (2009).
[11] C. H. Bennett, G. Brassard, S. Popescu, B. Schumacher, J. A. Smolin, and W. K. Wootters, Phys. Rev. Lett. **76**, 722 (1996).
[12] H. J. Briegel, W. Dür, J. I. Cirac, and P. Zoller, Phys. Rev. Lett. **81**, 5932 (1998).
[13] N. Sangouard, C. Simon, H. de Riedmatten, and N. Gisin, Rev. Mod. Phys. **83**, 33 (2011).
[14] M. Horodecki, P. W. Shor, and M. B. Ruskai, Rev. Math. Phys **15**, 629 (2003).
[15] A. S. Holevo, Russ. Math. Surv. **53**, 1295 (1999).
[16] P. W. Shor, Phys. Rev. A **52**, R2493 (1995).
[17] A. M. Steane, Proc. R. Soc. London, Ser. A **452**, 2551 (1996).
[18] B. M. Terhal, Rev. Mod. Phys. **87**, 307 (2015).
[19] T. Yu and J. H. Eberly, Quantum Inf. Comput. **7**, 459 (2007).
[20] P. Zanardi and M. Rasetti, Phys. Rev. Lett. **79**, 3306 (1997).
[21] D. A. Lidar, I. L. Chuang, and K. B. Whaley, Phys. Rev. Lett. **81**, 2594 (1998).
[22] L. Viola and S. Lloyd, Phys. Rev. A **58**, 2733 (1998).
[23] L. Viola and E. Knill, Phys. Rev. Lett. **94**, 060502 (2005).
[24] S. Damodarakurup, M. Lucamarini, G. Di Giuseppe, D. Vitali, and P. Tombesi, Phys. Rev. Lett. **103**, 040502 (2009).
[25] M. J. Biercuk, H. Uys, A. P. VanDevender, N. Shiga, W. M. Itano, and J. J. Bollinger, Nature (London) **458**, 996 (2009).
[26] A. Orieux, A. D'Arrigo, G. Ferranti, R. Lo Franco, G. Benenti, E. Paladino, G. Falci, F. Sciarrino, and P. Mataloni, Sci. Rep. **5**, 8575 (2015).
[27] A. De Pasquale and V. Giovannetti, Phys. Rev. A **86**, 052302 (2012).
[28] L. Lami and V. Giovannetti, J. Math. Phys. **56**, 092201 (2015).
[29] R. Alicki and K. Lendi, *Quantum Dynamical Semigroups and Applications* (Springer, Berlin, 1987).
[30] H. P. Breuer and F. Petruccione, *The Theory of Open Quantum Systems* (Oxford University Press, New York, 2002).
[31] W. K. Wootters, Phys. Rev. Lett. **80**, 2245 (1998).
[32] A. Fedrizzi, T. Herbst, A. Poppe, T. Jennewein, and A. Zeilinger, Opt. Express **15**, 15377 (2007).
[33] A. S. Holevo, Probl. Inf. Transm. **44**, 171 (2008).
[34] A. De Pasquale, A. Mari, A. Porzio, and V. Giovannetti, Phys. Rev. A **87**, 062307 (2013).
[35] L. M. Duan and C. Monroe, Rev. Mod. Phys. **82**, 1209 (2010).
[36] S. Ritter, C. Nölleke, C. Hahn, A. Reiserer, A. Neuzner, M. Uphoff, M. Mücke, E. Figueroa, J. Bochmann, and G. Rempe, Nature (London) **484**, 195 (2012).